metals

MDPI

Article

Precipitation Thermodynamics in an Al–Zn–Mg Alloy with Different Grain Sizes

Zhen Wang [1], Siqi Huang [1], Wenkai Zhang [1], Shunqiang Li [1] and Jizi Liu [1,2,*]

[1] Nano and Heterogeneous Materials Center, Nanjing University of Science and Technology, Nanjing 210094, China; 9201160d0312@njust.edu.cn (Z.W.); siqihuang@njust.edu.cn (S.H.); 9201160d0316@njust.edu.cn (W.Z.); shunqiangli@njust.edu.cn (S.L.)
[2] Center of Analytical Facilities, Nanjing University of Science and Technology, Nanjing 210094, China
* Correspondence: jzliu@njust.edu.cn

Abstract: In order to gain insight into the influence of grain size on precipitation thermodynamics, bulk materials of coarse-grained (CG), ultrafine-grained (UFG) (with or without dislocations), and nanocrystalline (NC) 7075 Al alloy have been fabricated by solid solution treatment, equal-channel angular pressing (ECAP), or high-pressure torsion (HPT) processes. The precipitation behavior and the corresponding thermal phenomenon were studied by transmission electron microscopy (TEM) and differential scanning calorimetry (DSC) heating. The results indicated that there are significant differences in precipitation thermodynamics among the four bulk materials. In the CG and UFG materials without dislocations, homogeneous nucleation is the primary precipitation mechanism. However, the nucleation of the GP zones is suppressed at lower temperatures due to a reduction in the number of residual vacancies and the supersaturation in the UFG interiors. This is attributed to the absorption of vacancies and solute atoms by a greater volume of grain boundaries. It can be observed that the greater the excess of vacancies remaining in grain interiors, the lower the temperature at which nucleation of GP zones occurs. Defect-assisted heterogeneous nucleation was identified as the predominant precipitation mechanism in the UFG materials with dislocations and the NC materials. These defects encompass dislocations, lattice distortions, and grain boundaries. The decomposition processes of solid solutions were found to be almost complete at a lower temperature. The presence of dislocations, lattice distortions, and grain boundaries enables solute atoms to diffuse at a much faster rate, significantly enhancing the precipitation rate and reducing the nucleation and formation energies of various precipitate phases.

Keywords: aluminum alloy; precipitation; thermodynamics; TEM

check for updates

Citation: Wang, Z.; Huang, S.; Zhang, W.; Li, S.; Liu, J. Precipitation Thermodynamics in an Al–Zn–Mg Alloy with Different Grain Sizes. *Metals* **2024**, *14*, 625. https://doi.org/10.3390/met14060625

Academic Editor: Andrey Pozdniakov

Received: 17 April 2024
Revised: 17 May 2024
Accepted: 18 May 2024
Published: 25 May 2024

1. Introduction

The strength of Al alloy is comparable with that of low-carbon steel, but its density is only one-third that of steel. Consequently, Al alloys, which exhibit high specific strength, are of significant economic value in the aerospace and automobile industries. Therefore, ultra-high strength has long been a key area of interest for researchers investigating lightweight aluminum alloys. Alloying for precipitation is a well-established and successful method for enhancing the strength of age-hardenable aluminum alloys [1]. Al–Zn–Mg alloys have emerged as the most promising candidates in this regard [2]. For instance, the yield strength of AA 7050 can reach 500 MPa, whereas the yield strength of AA 6061 is less than 300 MPa. During the aging process, a high density of solute-rich nano-sized particles precipitate, thereby strengthening the alloys. The precipitation kinetics and strengthening behavior of hardening phases in Al–Zn–Mg alloys have been the subject of considerable attention in recent decades, with a substantial body of research published in this area [3–9]. Another strengthening approach, which involves a reduction in grain size, has been extensively researched over the past few decades in accordance with the classical Hall-Petch relationship [10–15]. This strengthening mechanism is based on the accumulation of dislocations at grain boundaries (GBs), which impede the dislocation motion. It is well known that nanocrystalline (NC) and ultrafine-grained (UFG) metals exhibit significantly enhanced strength compared to their microcrystalline counterparts. A significant number of investigations have been conducted with the objective of elucidating the underlying mechanisms of grain refinement and related mechanical behaviors in pure metals [16–18]. More recently, research has extended to alloys, where the consideration of more complex microstructures is essential. For example, the migration enrichment of alloying elements with the assistance of additional dislocations, grain boundaries (GBs), and other defects in NC and UFG materials modifies the precipitation kinetics in alloys such as the Al–Zn–Mg system in comparison to their coarse-grained (CG) counterpart [19–22].

The simultaneous incorporation of precipitation hardening and grain refinement has been proposed and employed as an important strengthening strategy to improve the strength of Al–Zn–Mg alloys. This approach has been shown to result in an extremely high strength of ~1 GPa in NC 7075 Al alloys [10], with the ductility also being improved by the formation of the appropriate precipitates [23]. Thus, it is therefore evident that a clear comprehension of the coupling between precipitates and UFG or NC materials is of paramount importance [19,20,24–26]. On the one hand, there are significant differences in the size, chemistry, and spatial distribution of precipitates between UFG and CG bulk materials [27,28]. Conversely, the presence of fine precipitates on the GBs is beneficial to the structural stability of UFG and NC materials as it hinders GB migration [29,30]. In order to comprehend the coupling effect, it is essential to initially comprehend the precipitation kinetics and thermodynamics, which are influenced by the grain sizes.

Many attempts have been made to understand the precipitation sequences in Al–Zn–Mg alloys with CG structures, and general conclusions were drawn as a reference [31–33]:

$$\text{Solid solution} \rightarrow \text{GPI zones} \rightarrow \text{GPII zones } (\text{GP}_{\eta'}/\text{GP}_{\eta\text{p}}) \rightarrow \eta'/\eta_{\text{p}} \rightarrow \eta\text{-MgZn}_2$$

The equilibrium phase of η-$MgZn_2$ is a hexagonal lattice known as the C14 Laves phase (a = 0.521 nm and c = 0.860 nm) [34]. To date, fifteen types of orientation relationships between η precipitates and the Al matrix have been reported [35]. It is postulated that the metastable η' and η_p phases will undergo a transformation into the stable η-phase, potentially via different crystallographic approaches, given the distinct lattice structures of these phases. The $\eta_{\prime}$ phase is fully coherent with the Al matrix and has a hexagonal lattice with $a = 0.496$ nm and $c = 6d_{111\text{Al}} = 1.402$ nm [36]. The η_p phase is hexagonal with parameters $a = 0.496$ nm and $c \approx 4d_{111\text{Al}} = 0.935$ nm. It is characterized by an onside interface dislocation loop and typical double-panel Zn-rich interfaces [9,33]. It is possible to confuse it with the η_2 phase due to the similar orientation relationship with the matrix. The η_2 precipitates have an orientation relationship of $[10\text{-}10]_{\eta2}//[110]_{\text{Al}}$, $(0001)_{\eta2}//(1\text{-}11)_{\text{Al}}$, with a typical sandwich structure observed along $[110]_{\text{Al}}$ [35,37]. The $\text{GP}_{\eta'}$ and $\text{GP}_{\eta\text{p}}$ zones are precursors of the η' and η_p phases, respectively. Both are disk-like in structure, but $\text{GP}_{\eta\text{p}}$ zones are more readily identifiable due to their sandwich configuration and the fixed seven-atomic-layer thickness [32]. Spherical GPI zones are observed at the early stage of artificial aging at low temperature or natural aging, which are considered to be ordered clusters [38,39]. In fact, a small quantity of Mn and Cr is incorporated into Al–Zn–Mg alloys with the intention of reducing the detrimental effect of the impurities Fe and Si. This is achieved through the formation of Al(Fe,Mn,Cr) and $Al_5(Fe,Mn)Si_2$ phases [40,41]. Furthermore, $Al_{12}(Mn,Cr)$ precipitates are observed following solution treatment at 450 °C in cast Al–Zn–Mg–Cu alloys [41]. The presence of Cr-rich and Mn-rich phases has been demonstrated to enhance the tensile strength and toughness of the alloy.

It is commonly accepted that the manufacturing processes of UFG and NC materials have either accelerated or suppressed a specific stage of precipitation. It is widely acknowledged that severe plastic deformation, including equal-channel angular pressing (ECAP) and high-pressure torsion (HPT), represents the most effective approach for the production of bulk UFG and NC materials with high strength [42]. Zhao et al. [26] observed that the ECAP process resulted in a higher volume fraction of GP zones and a lower volume fraction of η′ precipitates in naturally aged UFG material than those in the naturally aged CG counterpart. The growth of precipitates during the ECAP process of a 7316 Al alloy at 200 °C was found to be 50 times faster than that during conventional aging at the same temperature for CG materials [43]. Zhang et al. [27] demonstrated that HPT at room temperature and 200 °C both induced the formation of the η phase in 7075 Al alloy. Hu et al. demonstrated that the differences in the decomposition processes in Al–Zn–Mg alloys with UFG or CG structures stem from the discrepancies in the defects involved, such as dislocations, vacancies, and GBs [28]. In the aged HPT samples, bimodal precipitates were observed. The smaller precipitates exhibited similar behavior to those of the CG material, while the larger ones were associated with crystalline defects and reached larger sizes at considerably lower temperatures and shorter times as compared to the CG counterpart [44]. A review of the published literature reveals that there has been a paucity of studies investigating the complete decomposition process of alloys with varying grain sizes. Some conflicting results have been reported in the literature, which are largely attributed to the differing compositions of the alloys and the absence of a comprehensive comparative analysis.

In the present work, a commercial 7075 Al alloy was processed by ECAP and HPT after solution treatment, resulting in the formation of UFG and NC structures, respectively. Then, the UFG and NC materials, as well as the conventional solid-solution-treated CG materials, were subjected to artificial aging using differential scanning calorimetry (DSC) heating. In this study, DSC, electron back-scattered diffraction (EBSD), and transmission electron microscopy (TEM), as well as scanning TEM (STEM) with Z contrast, were employed to study the precipitation sequence, with the aim of providing insight into the influence of grain size on precipitation phenomena.

2. Experimental Procedures

Commercial 7075 Al alloy rods with a chemical composition of Al-5.96Zn-2.51Mg-1.39Cu-0.30Mn-0.20Cr-0.50Fe-0.40Si (wt.%) were subjected to homogenization at 480 °C for 5 h, then quenched into water to form supersaturated solid solution (designated as CG-7075 Al). ECAP and HPT processing were performed immediately after quenching. A die with an intersecting channel angle of 90° and an outer arc angle of 45° was employed here to form a UFG structure using the Bc route at ambient temperature for 2 passes (referred to as UFG1-7075 Al) and at 250 °C for 6 passes (termed as UFG2-7075 Al), respectively. The microstructural evolution of 7075 Al alloys during ECAP procedure can be found in reference [26], which provides guidance on the ECAP sample preparation in this work. To ensure the microstructural homogeneity, the analysis area is taken from the center of the transverse section, perpendicular to the pressing direction. Disks of 20 mm in diameter and 1.5 mm in thickness, which were machined from the homogenized 7075 rods, were processed by HPT for 10 revolutions under a pressure of 6 GPa to form the NC 7075 Al sample (referred to as NC-7075 Al). The HPT process was conducted in accordance with the guidance set out in reference [23]. The microstructures were studied at positions where the distance from the center was greater than 5 mm to avoid the microstructural inhomogeneity in the near-center regime.

Small rectangles were sectioned from the above CG, UFG, and NC materials and subjected to thermal analysis in a differential scanning calorimeter DSC-7 (Perkin-Elmer, Waltham, MA, USA). The polished rectangles were sealed in Al pans and heated in a flowing Ar atmosphere at a constant heating rate of 20 °C/min. An additional empty Al pan was used as a reference. To study the decomposition processes of the supersaturated solid solution, some specimens were heated to exothermic and endothermic peak temperatures in the DSC machine and then quenched to room temperature at a cooling rate of 500 °C/min. The quenched specimens were then examined by TEM or STEM.

The EBSD samples were electropolished in a solution of 10% perchloric acid and alcohol at room temperature. EBSD examinations were performed at an operating voltage of 15 kV, an aperture of 120 mm, a working distance of 14 mm, and a step size of 0.4 µm. Specimens for TEM observations were prepared in the following manner: the rectangular pieces were ground down to 200 µm, after which 3 mm diameter disks were punched out directly from the pieces. The disks were then mechanically polished and thinned down to 50 µm, after which they were electropolished to a thickness of electron transparency using a twinjet TJ100-SE (LEBOscience, Jiangyin, China) until perforation with a 30% nitric acid solution in methanol at −25 °C and 20 V. If the specimens were not thin enough, they were further ion-milled using a Gatan Precision Ion Milling System (AMETEK, Pleasanton, CA, USA) with an accelerating voltage of 3 kV at a temperature below 35 °C. TEM examinations were performed using an FEI Titan G^2 80-300 TEM (Thermo Fisher Scientific, Waltham, MA, USA), which was equipped with an aberration corrector implemented below its objective lens for imaging and an energy dispersive spectrometer (EDS) for component analysis. In the TEM mode, an information resolution of 0.07 nm can be reached at 300 kV. In the STEM mode, a point resolution of 0.16 nm was designed at 300 kV. With a high-angle annular dark-field (HAADF) detector, the obtained image shows a Z-contrast (where Z represents the atomic number of the atoms in the specimen) proportional to $Z^{1.7\sim2.0}$. Here, the HAADF-STEM images were generated with a half-angle of 21.4 mrad for probe convergence and a collection inner semi-angle of 53 mrad. This configuration facilitates the visualization of Zn segregation, as Zn atoms exhibit a significantly higher brightness than Al and Mg atoms.

3. Experimental Results

3.1. Microstructures before DSC Analysis

Figure 1 shows the grain morphologies and substructures within the interior of the grains in the CG, UFG1, UFG2, and NC 7075 Al alloys prior to DSC treatment. The microstructure of the solution-treated CG alloy is revealed by EBSD analysis map (Figure 1a), which is composed of coarse equiaxed grains. Statistical analysis of the grains indicated an average grain size of about 37 µm (Figure 2a). A typical grain is magnified in Figure 1e, which revealed the presence of elliptical Cr (Mn)-rich and rod-like Mn-rich dispersion phase particles. The dark-field TEM image in Figure 1b reveals that the grains in the UFG1 alloy had been severely deformed, with a high density of dislocations (Figure 1f). The grain size distribution of the UFG1 alloy is illustrated in Figure 2b, where the mean grain size is estimated to be about 116 nm. The grains in the UFG2 alloy are predominantly polygonal in shape, as shown in Figure 1c. This indicates that dynamic recovery and recrystallization occurred during the ECAP process at 250 °C for six passes. The grain size statistic in Figure 2c indicates an average size of about 2 µm. Upon enlarging the grains (Figure 1g), a few dislocations were observed. Figure 1d shows the grain morphology of the NC alloy, while the grain size distribution is displayed in Figure 2d, with a mean grain size of about 45 nm. These nano-sized grains exhibited severe deformation, as evidenced by the substantial lattice distortion revealed by the strain-field contrast in Figure 1h.

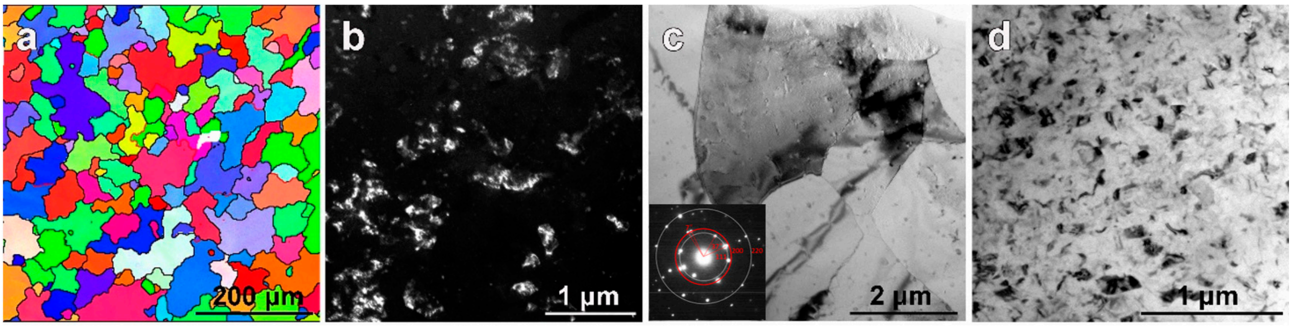

Figure 1. *Cont.*

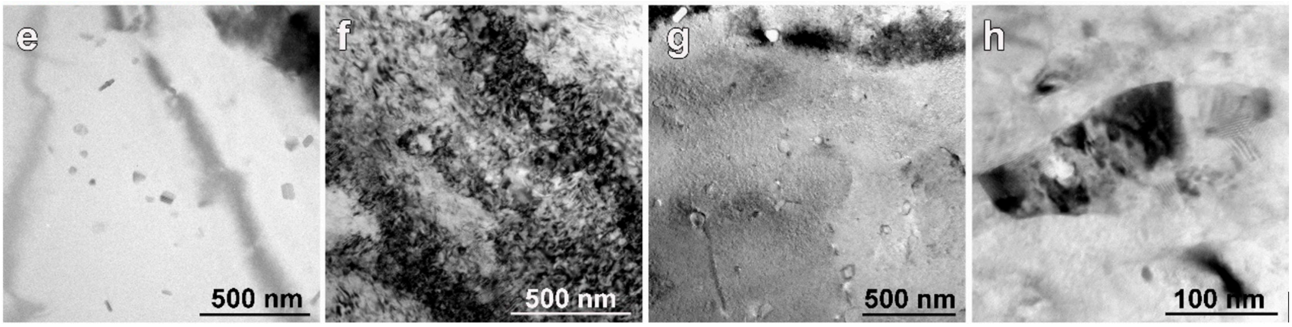

Figure 1. The grain structures in materials before DSC analysis: (**a**) the EBSD grain maps of the solid-solution-treated CG samples; black lines are high-angle grain boundaries with misorientation greater than 10°; (**b**) the dark-filed TEM micrograph of the UFG1 samples; (**c**,**d**) the brightfield TEM micrographs of the UFG2 samples and NC samples; the selected area electron diffraction (SAED) pattern in (**c**) several grains showing these grains have both high-angle grain boundary of 37° and low-angle grain boundary of 7°; (**e**–**h**) the brightfield TEM micrographs in the interior of grains in CG, UFG1, UFG2, and NC samples, respectively.

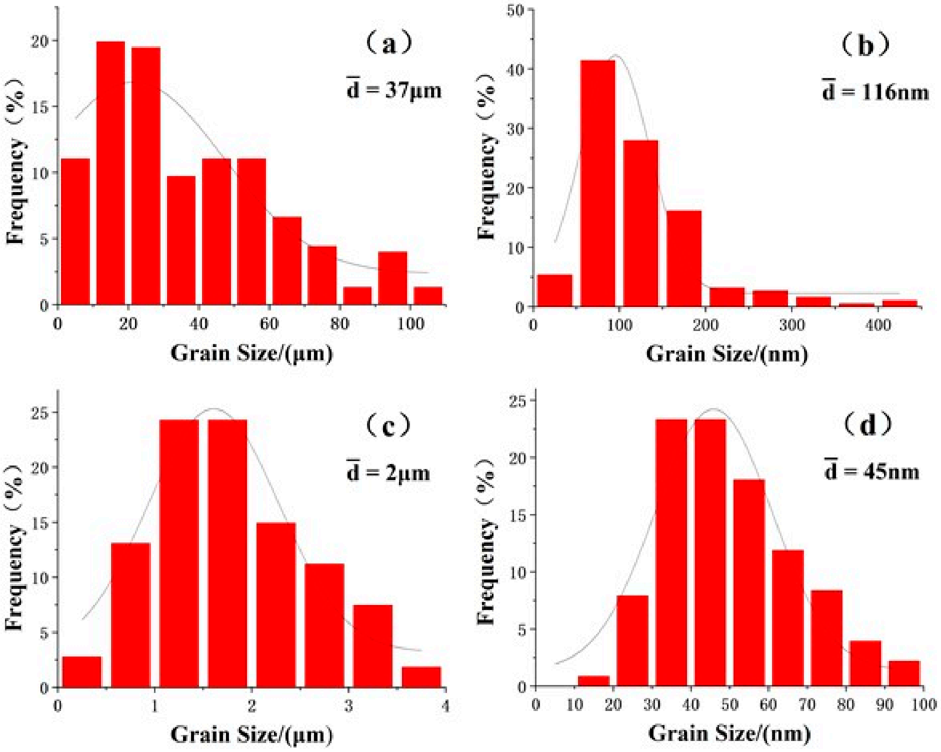

Figure 2. Grain size distribution before DSC analysis of (**a**) CG samples, (**b**) UFG1 samples, (**c**) UFG2 samples, and (**d**) NC samples.

3.2. Thermodynamic Data

As the result of the distinct grains, DSC thermograms of the CG, UFG1, UFG2, and NC 7075 Al alloys are integrated and compared in Figure 3. For all samples, the endothermic reactions occur in the same temperature range, spanning from about 100 to 190 °C (region I) and above 270 °C (region IV). The first endothermic peak is attributed to the dissolution of clusters and GPI zones [45,46], which were formed during the natural aging that occurred during storage. The principal differentiating factors are the peak areas and peak heights. The area of peak I for the NC specimen is considerably smaller than those for the CG and UFG specimens. This may be attributed to the presence of alloying atoms moving into a high density of grain boundaries in the NC materials, resulting in the formation of very small numbers of clusters and GPI zones. The starting dissolution temperature of peak I in the UFG materials is slightly higher than those in the NC and CG materials due to the enhanced stability of the clusters or GPI zones in the UFG materials. This is a consequence of the longer natural aging time for UFG specimens (4 years) compared to that of the CG and NC specimens (2 months) before DSC measurements were taken [38]. The second endothermic peak (region IV) is attributed to the re-dissolution of all precipitates, including the equilibrium η phase.

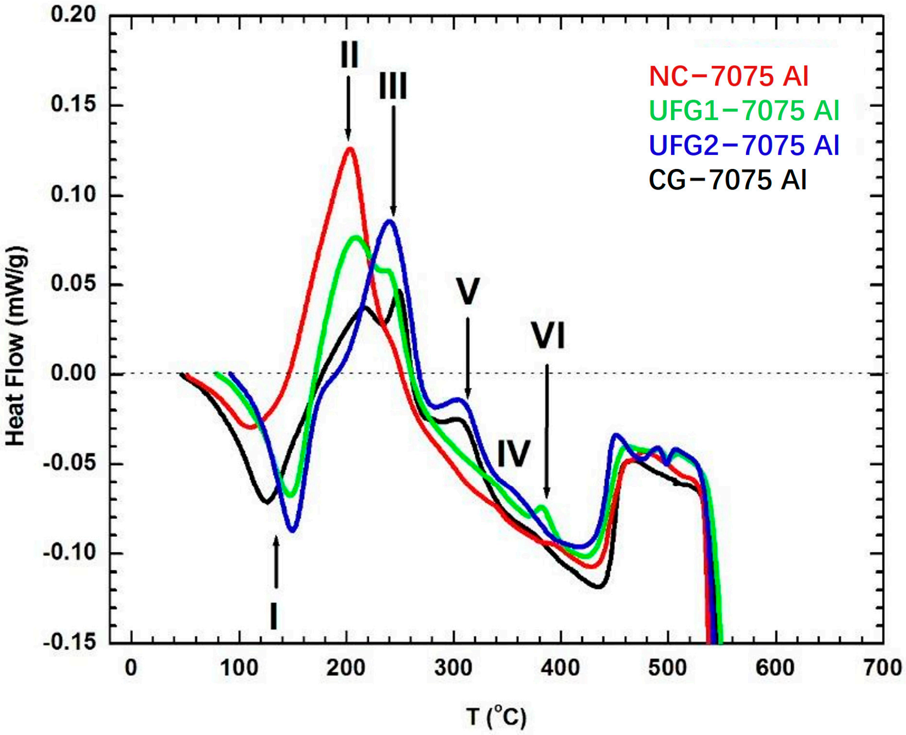

Figure 3. DSC thermogram of CG, UFG1, UFG2, and NC 7075 Al materials as quenched or as processed, respectively.

The significant differences in DSC analysis for different materials are manifested in exothermic peaks, which are closely related to precipitation thermodynamics. For CG materials, the three exothermic peaks are respectively located in the temperature range from 180 to 230 °C (region II), from 230 to 260 °C (region III), and from 280 to 360 °C (region V). As reported, these three peaks are believed to be related to GPII zones, η′ precipitates, and the η phase, respectively [45]. The second exothermic peak is of greater magnitude and narrower in width than the first, indicating that the η′ precipitates are more stable than the GPII zones. Moreover, the nucleation energy of the η′ precipitates is higher than that of the GPII zones in the case of homogeneous nucleation. The third exothermic peak is superimposed upon the second endothermic peak as a result of the transformation of the more stable precipitates into the η phase accompanied by the dissolution of the less stable precipitates into the matrix.

In the case of the UFG1 materials, three exothermic peaks are also observed, respectively, in the range from 170 to 220 °C (region II), from 220 to 270 °C (region III), and from 360 to 430 °C (region V). Peak II is higher than peak III; in other words, the first exothermic peak is fostered, while the second one is suppressed. This contrasts with the behavior observed in the CG materials. This anomalous phenomenon, in comparison with the CG counterpart, is attributed to the extreme intracrystalline lattice distortion, as shown in Figure 1b,f. Furthermore, this distortion postpones the occurrence of peak VI, i.e., the formation of the η phase.

The three exothermic peaks of the UFG2 materials exhibit a similar trend to those of the CG counterpart, with peaks observed in the range from 180 to 200 °C (region II), from

200 to 270 °C (region III), and from 260 to 340 °C (region V). In contrast, peak II is observed to be even more suppressed, while peak III is enhanced to a greater extent.

The three exothermic peaks of the NC materials, analogous to those of the UFG1 counterpart, are situated within the range from 140 to 230 °C (region II), from 230 to 260 °C (region III), and from 380 to 430 °C (region V). However, peak II of the NC materials is significantly enhanced, while peak III is almost extinct in comparison with the UFG1 counterpart.

Although the DSC results revealed the existence of thermodynamic differences among materials with different grain sizes, the relationship between the heat released and the phase transformation during precipitation remains unknown. TEM examination was employed to provide direct evidence of what is happening at the exothermic peaks.

3.3. Precipitates in the Interior of Grains before or after DSC Treatment

Figure 4 shows precipitates in the CG materials after DSC treatment, cutting off at each exothermic peak end. Prior to the DSC treatment, the as-received materials were subjected to a supersaturated solid-solution treatment, resulting in the formation of coarse grains. Following quenching, a significant number of vacancies remained. As shown in Figure 4a, a high density of precipitates is observed to be evenly distributed within the grains of the CG materials after DSC treatment, with cut-off at 220 °C. The high-resolution HAADF-STEM image with Z contrast in Figure 4d reveals that these precipitates are mainly $GP_{\eta'}$ zones with uniform contrast, with a few being $GP_{\eta p}$ zones with sandwich contrast. Further heating will result in the growth and coarsening of these GP zones, as observed in Figure 4b, taken from a CG specimen after DSC treatment and cut-off at 260 °C. Meanwhile, a phase transformation process from GP zones to metastable η' occurs, with a considerable number of η' precipitates being trapped with the lattice parameter $c = 6d_{111Al}$, as shown in Figure 4e. The η phase is found to be the predominant precipitate in the DSC-treated specimen cut-off at 360 °C, as presented in Figure 4c. A typical η_{11} precipitate is characterized in Figure 4f, where the inserted SAED pattern reveals the orientation relationship between η_{11} phase and Al matrix: $(0001)_{\eta 11}//(110)_{\mathrm{Al}}$, $[10\bar{1}0]_{\eta 11}//[1\bar{1}\bar{1}]_{\mathrm{Al}}$. It is apparent that the TEM characterizations provide the direct evidence for the above conjecture regarding the DSC–precipitation relationship: the formation of GP zones, η', and η phase, respectively, correspond to three exothermic peaks on the DSC curve in Figure 1.

The microstructures in the UFG1 materials before and after DSC treatment are shown in Figure 5. Figure 5a reveals that there is a small amount of precipitate in the as-received ECAP materials, identified as the η_p phase according to the red boxed unit cell in Figure 5e. The dense dislocations and lattice distortions produced by ECAP provide nucleation sites for these precipitates [47]. The dislocations can serve as effective diffusion pathways for atoms in a crystalline lattice, and this elemental migration mechanism is known as “pipe diffusion” [48]. Here, the diffusion of Zn and Mg atoms in the Al crystal lattice is a thermally activated process that can be strongly accelerated by dislocations and lattice distortions, resulting in the dynamic precipitation of the η_p phase during ECAP. After DSC treatment with cut-off at 210 °C, as shown in Figure 5b, it was found that there are bimodal-sized precipitates inside the grains and a larger η phase at the grain boundaries. The larger precipitates (indicated by red arrows) are identified as η_p phase and the smaller precipitates (indicated by black arrows) are confirmed as $GP_{\eta'}$ zones, as shown in Figure 5f. It can be inferred that the larger η_p phase originates from the previous smaller η_p phase in the as-received ECAP samples (Figure 5a). The smaller $GP_{\eta'}$ zones are newly formed during the DSC treatment by homogeneous nucleation in the dislocation-free region. These $GP_{\eta'}$ zones evolve into larger η' precipitates after DSC treatment, which is cut off at 260 °C, maintaining the orientation relationship with the Al matrix: $(0001)_{\eta'}//(111)_{\mathrm{Al}}$, $[10\bar{1}0]_{\eta'}//[110]_{\mathrm{Al}}$, as evidenced by the SAED pattern and the broad surface of disk-like η' precipitates lying on $\{111\}_{\mathrm{Al}}$ planes, indicated by the red lines in Figure 5c. In addition to the evolution of precipitates, the exothermic peak is partly contributed by recrystallization, which is implied by the widespread polygonal sub-grains in the specimens, as shown in Figure 5g.

In samples treated by DSC heating with cut-off at 430 °C, a large number of large η particles are observed in Figure 5d, where the inserted SAED pattern shows a certain rotation angle occurring between η phase and Al matrix around the $<112>_{Al}$ zone axis compared to the orientation relationship between η′ phase and Al matrix. In addition, the grains are found to be sharply coarsened in the micrometer range, as indicated in Figure 5h.

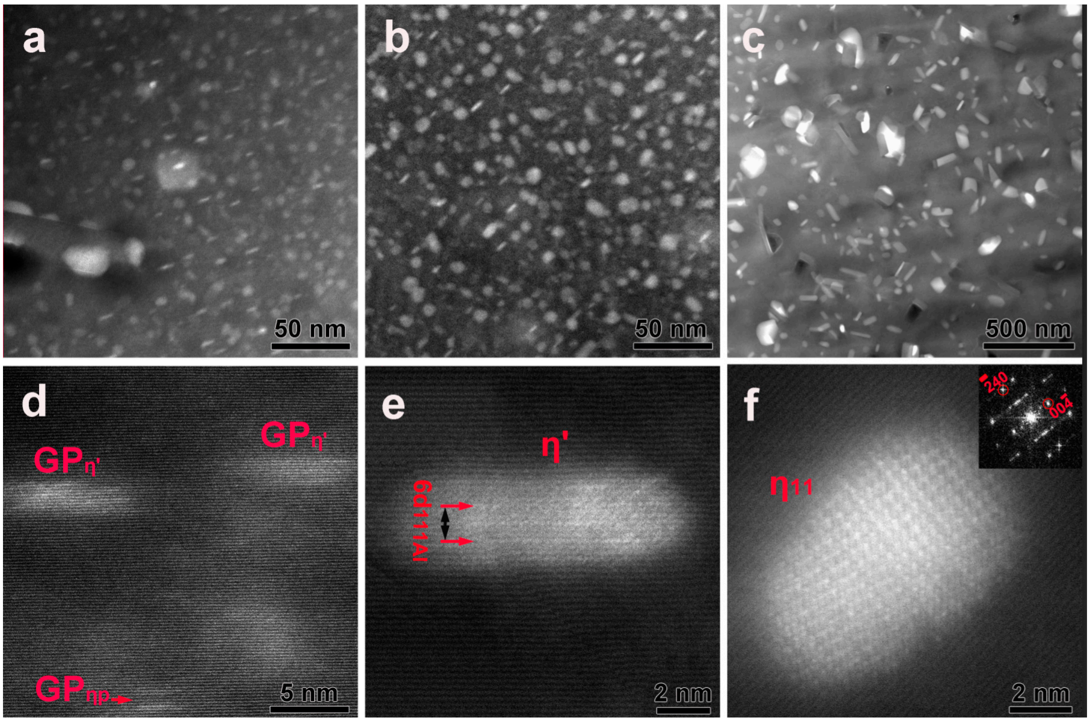

Figure 4. The HAADF-STEM images of precipitates viewed along $<112>_{Al}$ in CG materials after DSC treatment cut-off at (**a**) 220 °C, (**b**) 260 °C, and (**c**) 360 °C, respectively. The selected typical and representative precipitates in (**a**–**c**) are enlarged in (**d**–**f**), respectively, showing their crystallographic features.

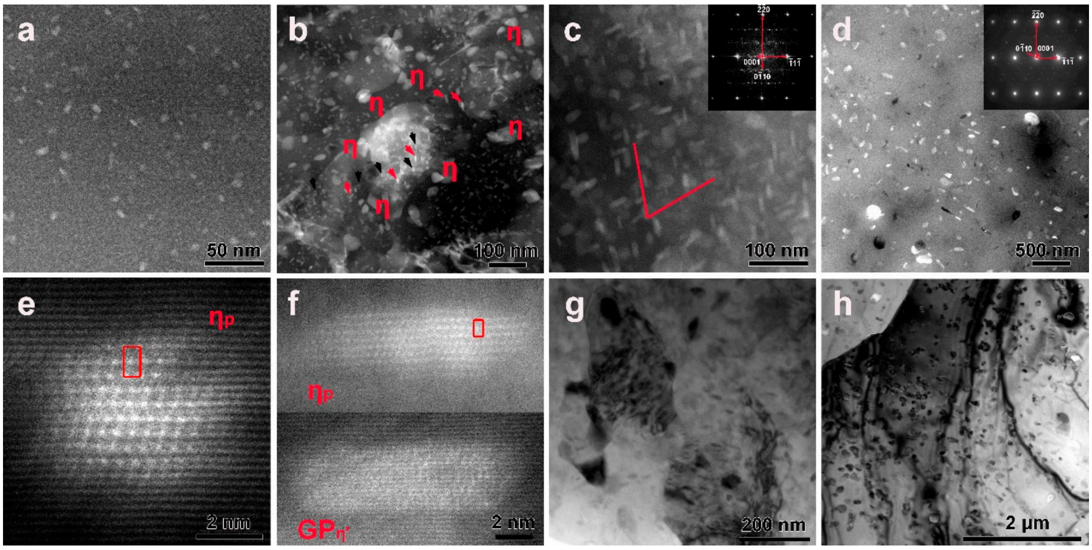

Figure 5. The HAADF-STEM images of precipitates in UFG1 materials before (**a**) or after DSC treatment cut-off at (**b**) 210 °C, (**c**) 260 °C, and (**d**) 430 °C, respectively. The selected typical and representative precipitates in (**a**,**b**) are enlarged in (**e**,**f**), respectively, showing their crystallographic features. The insets in (**c**,**d**) are SAED patterns from a particle in (**c**,**d**). The grains under the condition of (**c**,**d**) are shown in the brightfield TEM images of (**g**,**h**).

Figure 6 shows precipitates inside the grains of the UFG2 materials after DSC treatment cut-off at 190 °C, 270 °C, and 300 °C, respectively. The HAADF-STEM images in Figure 6a,d show no precipitate inside the grains in the UFG2 materials after DSC treatment cut-off at 190 °C; Zn elemental atoms are found to be enriched at grain boundaries and the arrowed (Cr, Mn)-rich phase boundaries. After cut-off at a higher temperature of 270 °C, Figure 6b shows a high density of precipitates forming inside the grains, most of which are η' phase, and a few are η_p phase, as indicated by the arrows and confirmed by the high-resolution TEM images in Figure 6e. The η_p precipitates are selectively located near defects, such as dislocations and grain or phase boundaries, while the η' precipitates are diffusely distributed inside defect-free grains. In the samples cut off at 300 °C, a huge amount of precipitate is observed in Figure 6c, but only a part of it is stable η phase, as revealed by the inserted SAED pattern and the corresponding dark-field TEM image in Figure 6f, and the other part is still the metastable phase with small size.

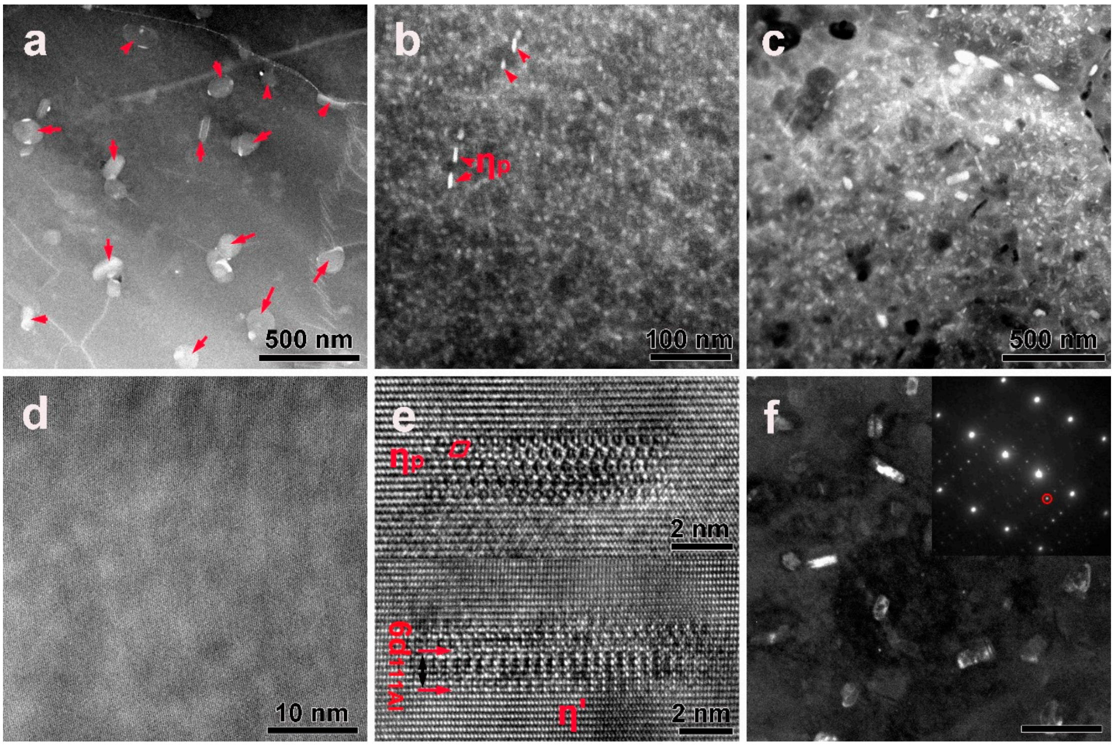

Figure 6. The HAADF-STEM images of precipitates in UFG2 materials after DSC treatment cut-off at (**a**) 190 °C, (**b**) 270 °C, and (**c**) 300 °C, respectively. The selected typical and representative precipitates in (**a**–**c**) are enlarged in (**d**–**f**), respectively, showing their crystallographic features, even with the help of SAED pattern, as illustrated in (**f**).

Figure 7 shows the microstructures of HPT NC materials before and after DSC treatment. In the HPT processed samples, numerous η precipitates are observed at the abundant grain boundaries (Figure 7a), while a few η_p precipitates are found inside grains (Figure 7e). During HPT, a lot of alloying elements (Zn and Mg) were transported into grain boundaries by dislocations, resulting in the accumulation of large quantities of Zn and Mg atoms at these boundaries. Thus, the concentration of alloying elements within the interior of grains is relatively low. Nevertheless, some Zn-rich η_p precipitates have been observed to form inside grains. This is largely attributed to lattice distortion accelerating the segregation of alloying elements. Following the DSC treatment cut-off at 200 °C, the topography of nano-grains surrounded by the large η precipitates is shown in Figure 7b. The bimodal-sized precipitates can be observed inside the grains; the larger ones are confirmed to be η_p particles, and the smaller ones are $GP_{\eta'}$ zones, identified by high-resolution HAADF-STEM images with Z contrast in Figure 7f. Figure 7c shows precipitates in materials after DSC treatment cut-off at 260 °C. Obviously, only large stable η precipitates with subglobular morphology remain. In contrast, the small metastable precipitates have been re-dissolved into the matrix. Another notable feature is recrystallization, as shown in the dark-field TEM image in Figure 7g, where the grains exhibit an equiaxed morphology. After DSC treatment cut-off at 430 °C, most of the precipitates had been re-dissolved (Figure 7d), and the grains had undergone significant coarsening (Figure 7h).

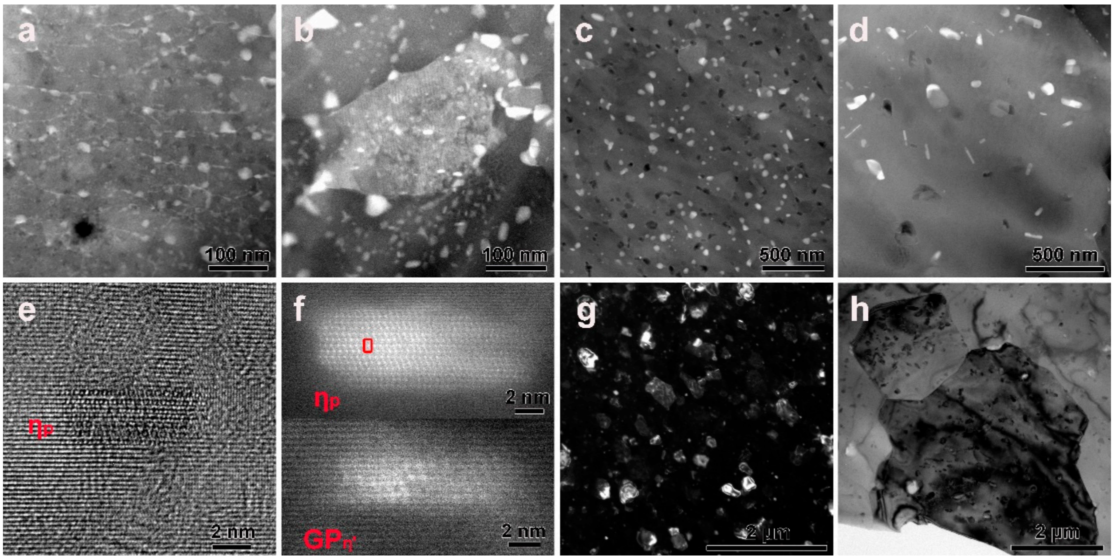

Figure 7. Precipitates in NC materials before (**a**) or after DSC treatment cut-off at (**b**) 200 °C, (**c**) 260 °C, and (**d**) 430 °C, respectively. The selected typical and representative precipitates in (**a**,**b**) are enlarged in (**e**,**f**), respectively, showing their crystallographic features. The grains under the condition of (**c**,**d**) are shown in (**g**,**h**).

4. Discussion

The results presented in this work indicate that there are significant differences in the exothermic peaks. However, the endothermic reactions among specimens with different grain sizes and grain structures during DSC heating are similar, as summarized in Figure 3. As is well known in the field of Al–Zn–Mg alloys, the endothermic reaction is believed to be mainly contributed by the dissolution of precipitates, while the exothermic peak is closely related to the precipitation, phase transformation, and defect recovery. TEM observations provide direct evidence for the analysis of thermodynamic features that have been detected by DSC measurement. The differences in grain size, resulting from either deformation processing or heat treatment procedures, were accompanied by the changes in the grain substructures, including dislocations and grain boundaries. These changes influenced the precipitation thermodynamics and kinetics. For instance, a high density of dislocations and lattice distortions was observed in the UFG1 specimens, whereas dislocations in the UFG2 specimens were totally annealed, resulting in the difference in precipitation behavior and thereby the exothermic peaks of the DSC curves. A high density of dislocations will enhance the precipitation kinetics, resulting in an acceleration in the nucleation and growth of precipitates [28]. For example, during ECAP processing, the high density of mobile dislocations serves as fast diffusion paths for solute atoms in the processes of the nucleation or growth of precipitates.

The precipitation sequence is well documented in the literature as occurring in seven Al–Zn–Mg alloys during artificial aging, which can be described as [9,31,49]: supersaturated solid solution (SSSS) → GP zones → η' → η-$MgZn_2$. This decomposition reaction commences with the homogeneous nucleation of GP zones, which is highly dependent on the excess vacancy concentration [50–53]. However, in an Al matrix with dense dislocations, lattice distortions, and boundaries, the above decomposition reactions will be changed by heterogeneous nucleation due to the segregation of solute atoms and the critical influence of fast diffusion near these defects on nucleation thermodynamics and kinetics. Hence, to rationalize the DSC results for the materials with different grain sizes, the discussion will now turn to the impact of defects on precipitation thermodynamics.

4.1. The Precipitation Thermodynamics in CG and UFG2 Materials

The precipitation sequences observed in the CG specimens involve the decomposition of the supersaturated solid solution, commencing with the formation of GP zones, which subsequently transform into metastable η' or η_p transition phases and eventually into the equilibrium η phase. These three aforementioned steps become increasingly thermally stable with each subsequent stage, occurring at progressively higher temperature, which displays three exothermic peaks (II, III, and V) on the DSC curves in Figure 1. This correspondence has been proved directly by the TEM results (Figure 4).

However, the aforementioned correspondence has changed in the UFG2 specimens. The first exothermic peak for the UFG2 specimens was greatly inhibited, while the second exothermic peak was significantly promoted. A comparison of Figure 6a with Figure 4a reveals that the density of the GP zones is significantly lower in the UFG2 materials than that in the CG counterpart. This phenomenon can be explained by the denudation of vacancies in the UFG2 microstructure, which is characterized by a lower supersaturation of solute atoms inside grains [28]. The UFG2 specimen was produced by ECAP at 250 °C for six passes: (1) the low quenching rate generates only a few vacancies; (2) a higher volume of grain boundaries (GBs) act as sinks to absorb vacancies and cause annihilation; (3) the formation of a great number of grain boundary precipitates (GPBs) cause rapid depletion of matrix solute and thereby lead to a very low supersaturation of Mg and Zn in grain interiors. As shown in Figure 1e,g, a few dislocations are observed in both the CG and UFG2 specimens. This suggests that the nucleation and growth of the GP zones is predominantly controlled by homogeneous nucleation, which is highly dependent on the excess vacancy concentration. In order for nucleation and growth to occur, a specific critical vacancy concentration and a higher supersaturation of solute atoms are required at an aging temperature below which nucleation does not occur. This is evidenced by the low density of precipitates observed in the UFG2 sample at the first exothermic peak. As the aging temperature increases towards the second exothermic peak, the GP zones begin to nucleate and grow. Concurrently, the phase transformation from the GP zones to η' or η_p occurs. It is thought to be the reason why the second exothermic peak is greatly promoted in the UFG2 material in comparison with that of the CG counterpart. A comparison of Figures 6c and 4c reveals that the majority of precipitates in the UFG2 specimens are much smaller than those in the CG counterpart, with the exception of those on dislocations or at grain boundaries. Given that the UFG2 material possesses a greater volume of GBPs than its counterpart, it can be postulated that the depletion of matrix solute will result in a lower supersaturation of Mg and Zn in the UFG materials. Consequently, the growth of η precipitates in regions distant from dislocations and GBs is likely to be impeded.

4.2. The Precipitation Thermodynamics in NC and UFG1 Materials

The DSC results in Figure 3 reveal that the precipitation thermodynamics is similar in the NC and UFG1 materials but different from the CG and UFG2 materials. This difference is mainly due to a large number of defects in the NC and UFG1 materials. Precipitates formed by homogeneous nucleation mechanisms have been documented as the main precipitation mechanism in CG and UFG2 materials with the absence of dislocations in the grain interiors. However, in the NC and UFG1 materials, defects such as dislocations, lattice distortions, and GBs (see Figure 1f,h) become the main nucleation sites promoting heterogeneous nucleation. In this case, the precipitation nucleation kinetics will be critically affected by the segregation of solute atoms and their fast diffusion on or near these defects. Therefore, the first exothermic peak is more pronounced at lower temperatures in the NC and UFG1 materials as opposed to the CG and UFG2 specimens.

Before the DSC treatment, the formation of precipitates was observed at GBs and near dislocation cores in the NC and UFG1 specimens (Figures 5a and 7a). The majority of these precipitates demonstrated thermal stability, with the capacity to withstand dissolution at the first endothermic peak temperature. These precipitates are stable GP zones, η' or η_p, or the η phase. The equilibrium η phase can nucleate directly from the solid solution with the assistance of lattice distortions and GBs [5,20,27]. At the first exothermic peak temperature, the conventional precipitation sequences are nearly complete, especially in NC grains. A significant amount of heat is released to make the first exothermic peaks more pronounced. Most precipitations (including nucleation and phase transformation) have been completed at the first exothermic peak, resulting in a significant weakening of the second exothermic peak, particularly in the NC materials, which has largely disappeared. The TEM results have also revealed that the second and the third exothermic peaks are not directly related to precipitation but rather to the recovery and recrystallization of UFGs and nano-grains (NGs).

4.3. The Precipitation Thermodynamics Affected by ECAP and HPT Processes

As discussed above, the precipitation thermodynamics are predominantly influenced by the grain structures. Although the grain structures are produced by ECAP and HPT processing, it is challenging to establish a direct correlation between the processing methods and the precipitation. For example, both the UFG1 and UFG2 samples are produced by ECAP processing, yet they exhibit entirely disparate precipitation pathways. A high density of dislocations or lattice distortions is observed in the UFG1 samples; however, dynamic recovery and recrystallization occurs, resulting in defect annihilation in the UFG2 samples. This difference in defect density makes different precipitation paths. The precipitation dynamics of the HPT NC samples is comparable to that of the ECAP UFG1 samples given that they exhibit a similar defect density.

5. Conclusions

The coarse-grained (CG), ultrafine-grained (UFG) (with or without dislocations), and nanocrystalline (NC) 7075 Al alloy bulk materials were prepared by solid solution treatment, equal-channel angular pressing, or high-pressure torsion processes. The precipitation thermodynamics of these materials was studied by transmission electron microscopy and differential scanning calorimetry (DSC), and the following conclusions can be drawn:

(1) Homogenous nucleation is conformed to be the main precipitation mechanism in the CG and UFG2 materials, and the formation of GP zones is highly dependent on the excess vacancy concentration. The three steps during the decomposition of the supersaturated solid solution can be revealed by three clear exothermic peaks on the DSC curves for the CG materials.

(2) The nucleation of the GP zones in the UFG2 materials has been suppressed significantly at the first exothermic peak temperature due to the fewer vacancies remaining and the lower supersaturation in grain interiors. These disappeared vacancies and solute atoms have been absorbed by a higher volume of grain boundaries. Thus, the nucleation will occur at high temperature and make contributions to the second exothermic peak, along with the phase transformation from the GP zones to metastable phases.

(3) The whole decomposition processes of the solid solution have been nearly completed in the first exothermic peak; the other two exothermic peaks are more attributed to the recovery and recrystallization of the UFGs and NGs in the UFG1 and NC materials. The defect-assisted heterogeneous nucleation is confirmed to be the main precipitation mechanism, and these defects involve dislocations, lattice distortions, and grain boundaries.

(4) It is found that the more excess vacancies remaining in the grain interiors, the lower the temperature of the nucleation of the GP zones.

Author Contributions: Z.W.: Investigation, Formal analysis, Visualization, Writing—original draft, Validation; S.H., W.Z., and S.L.: Formal analysis, Writing—original draft, Writing—review and editing, Validation; J.L.: Conceptualization, Methodology, Formal analysis, Writing—review and editing, Supervision, Project administration, Funding acquisition, Validation. All authors have read and agreed to the published version of the manuscript.

Funding: This work was funded by the National Natural Science Foundation of China (52171119), the Fundamental Research Funds for the Central Universities (No. 2023201001), and the Natural Science Foundation of Jiangsu Province (BK20201308). The authors are thankful for the technical support from the Jiangsu Key Laboratory of Advanced Micro and Nano Materials and Technology and the Analysis and Test Center of Nanjing University of Science and Technology.

Data Availability Statement: The raw data supporting the conclusions of this article will be made available by the authors on request.

Conflicts of Interest: The authors declare that they have no known competing financial interests or personal relationships that could have appeared to influence the work reported in this paper.

References

1. Chen, Y.-Q.; Xu, J.-B.; Pan, S.-P.; Li, N.-B.; Ou, C.-G.; Liu, W.-H.; Song, Y.-F.; Tan, X.-R.; Liu, Y. Effect of T6I6 treatment on dynamic mechanical behaviour of Al-Si-Mg-Cu cast alloy and impact resistance of its cast motor shell. *J. Cent. South Univ.* **2022**, *29*, 924–936. [CrossRef]
2. Hornbogen, E. Hundred years of precipitation hardening. *J. Light Met.* **2001**, *1*, 127–132. [CrossRef]
3. Matsuda, K.; Yasumoto, T.; Bendo, A.; Tsuchiya, T.; Lee, S.; Nishimura, K.; Nunomura, N.; Marioara, C.D.; Levik, A.; Holmestad, R.; et al. Effect of Copper Addition on Precipitation Behavior near Grain Boundary in Al-Zn-Mg Alloy. *Mater. Trans.* **2019**, *60*, 1688–1696. [CrossRef]
4. Cassell, A.M.; Robson, J.D.; Race, C.P.; Eggeman, A.; Hashimoto, T.; Besel, M. Dispersoid composition in zirconium containing Al-Zn-Mg-Cu (AA7010) aluminium alloy. *Acta Mater.* **2019**, *169*, 135–146. [CrossRef]
5. Zhao, H.; De Geuser, F.; da Silva, A.K.; Szczepaniak, A.; Gault, B.; Ponge, D.; Raabe, D. Segregation assisted grain boundary precipitation in a model Al-Zn-Mg-Cu alloy. *Acta Mater.* **2018**, *156*, 318–329. [CrossRef]
6. Santos, J.F.D.; Staron, P.; Fischer, T.; Robson, J.D.; Kostka, A.; Colegrove, P.; Wang, H.; Hilgert, J.; Bergmann, L.; Hütsch, L.L.; et al. Understanding precipitate evolution during friction stir welding of Al-Zn-Mg-Cu alloy through in-situ measurement coupled with simulation. *Acta Mater.* **2018**, *148*, 163–172. [CrossRef]
7. Gumbmann, E.; De Geuser, F.; Sigli, C.; Deschamps, A.; Mg, I.O. Ag and Zn minor solute additions on the precipitation kinetics and strengthening of an Al-Cu-Li alloy. *Acta Mater.* **2017**, *133*, 172–185. [CrossRef]
8. Deschamps, A.; Fribourg, G.; Bréchet, Y.; Chemin, J.L.; Hutchinson, C.R. In situ evaluation of dynamic precipitation during plastic straining of an Al–Zn–Mg–Cu alloy. *Acta Mater.* **2012**, *60*, 1905–1916. [CrossRef]
9. Liu, J.Z.; Chen, J.H.; Yang, X.B.; Ren, S.; Wu, C.L.; Xu, H.Y.; Zou, J. Revisiting the precipitation sequence in Al–Zn–Mg-based alloys by high-resolution transmission electron microscopy. *Scr. Mater.* **2010**, *63*, 1061–1064. [CrossRef]
10. Liddicoat, P.V.; Liao, X.-Z.; Zhao, Y.; Zhu, Y.; Murashkin, M.Y.; Lavernia, E.J.; Valiev, R.Z.; Ringer, S.P. Nanostructural hierarchy increases the strength of aluminium alloys. *Nat. Commun.* **2010**, *1*, 63. [CrossRef]
11. Zha, M.; Li, Y.; Mathiesen, R.H.; Bjørge, R.; Roven, H.J. Microstructure evolution and mechanical behavior of a binary Al–7Mg alloy processed by equal-channel angular pressing. *Acta Mater.* **2015**, *84*, 42–54. [CrossRef]
12. Mulyukov, R.R.; Imayev, R.M.; Nazarov, A.A. Production, properties and application prospects of bulk nanostructured materials. *J. Mater. Sci.* **2008**, *43*, 7257. [CrossRef]
13. Du, C.; Jin, S.; Fang, Y.; Li, J.; Hu, S.; Yang, T.; Zhang, Y.; Huang, J.; Sha, G.; Wang, Y.; et al. Ultrastrong nanocrystalline steel with exceptional thermal stability and radiation tolerance. *Nat. Commun.* **2018**, *9*, 5389. [CrossRef] [PubMed]
14. Zhou, X.; Feng, Z.; Zhu, L.; Xu, J.; Miyagi, L.; Dong, H.; Sheng, H.; Wang, Y.; Li, Q.; Ma, Y.; et al. High-pressure strengthening in ultrafine-grained metals. *Nature* **2020**, *579*, 67–72. [CrossRef] [PubMed]
15. Cheng, Z.; Zhou, H.; Lu, Q.; Gao, H.; Lu, L. Extra strengthening and work hardening in gradient nanotwinned metals. *Science* **2018**, *362*, eaau1925. [CrossRef] [PubMed]
16. Ovid, I.A.; Valiev, R.Z.; Zhu, Y.T. Review on superior strength and enhanced ductility of metallic nanomaterials. *Prog. Mater. Sci.* **2018**, *94*, 462–540. [CrossRef]
17. Valiev, R.Z.; Estrin, Y.; Horita, Z.; Langdon, T.G.; Zehetbauer, M.J.; Zhu, Y.T. Fundamentals of Superior Properties in Bulk NanoSPD Materials. *Mater. Res. Lett.* **2016**, *4*, 1–21. [CrossRef]
18. Wu, X.L.; Zhu, Y.T.; Wei, Y.G.; Wei, Q. Strong Strain Hardening in Nanocrystalline Nickel. *Phys. Rev. Lett.* **2009**, *103*, 205504. [CrossRef] [PubMed]
19. Ma, K.; Wen, H.; Hu, T.; Topping, T.D.; Isheim, D.; Seidman, D.N.; Lavernia, E.J.; Schoenung, J.M. Mechanical behavior and strengthening mechanisms in ultrafine grain precipitation-strengthened aluminum alloy. *Acta Mater.* **2014**, *62*, 141–155. [CrossRef]

20. Ma, K.; Hu, T.; Yang, H.; Topping, T.; Yousefiani, A.; Lavernia, E.J.; Schoenung, J.M. Coupling of dislocations and precipitates: Impact on the mechanical behavior of ultrafine grained Al–Zn–Mg alloys. *Acta Mater.* **2016**, *103*, 153–164. [CrossRef]
21. Sun, W.; Zhu, Y.; Marceau, R.; Wang, L.; Zhang, Q.; Gao, X.; Hutchinson, C. Precipitation strengthening of aluminum alloys by room-temperature cyclic plasticity. *Science* **2019**, *363*, 972–975. [CrossRef] [PubMed]
22. Jia, D.-S.; He, T.; Song, M.; Huo, Y.-M.; Du, X.-Y.; Vereshchaka, A.; Li, J.; Hu, H.-Y. Microstructure evolution of 7050 Al alloy fasteners during cold upsetting after equal channel angular pressing. *J. Cent. South Univ.* **2023**, *30*, 3682–3695. [CrossRef]
23. Zhao, Y.H.; Liao, X.Z.; Cheng, S.; Ma, E.; Zhu, Y.T. Simultaneously Increasing the Ductility and Strength of Nanostructured Alloys. *Adv. Mater.* **2006**, *18*, 2280–2283. [CrossRef]
24. Huo, W.; Guo, M.; Hou, L.; Cui, H.; Sun, T.; Zhuang, L.; Zhang, J. Progress on Research of Advanced Thermo-mechanical Treatment of Aluminum Alloy. *J. Mater. Sci. Eng.* **2014**, *32*, 284.
25. Zhang, S.; Hu, W.; Berghammer, R.; Gottstein, G. Microstructure evolution and deformation behavior of ultrafine-grained Al–Zn–Mg alloys with fine η′ precipitates. *Acta Mater.* **2010**, *58*, 6695–6705. [CrossRef]
26. Zhao, Y.H.; Liao, X.Z.; Jin, Z.; Valiev, R.Z.; Zhu, Y.T. Microstructures and mechanical properties of ultrafine grained 7075 Al alloy processed by ECAP and their evolutions during annealing. *Acta Mater.* **2004**, *52*, 4589–4599. [CrossRef]
27. Zhang, Y.; Jin, S.; Trimby, P.W.; Liao, X.; Murashkin, M.Y.; Valiev, R.Z.; Liu, J.; Cairney, J.M.; Ringer, S.P.; Sha, G. Dynamic precipitation, segregation and strengthening of an Al-Zn-Mg-Cu alloy (AA7075) processed by high-pressure torsion. *Acta Mater.* **2019**, *162*, 19–32. [CrossRef]
28. Hu, T.; Ma, K.; Topping, T.D.; Schoenung, J.M.; Lavernia, E.J. Precipitation phenomena in an ultrafine-grained Al alloy. *Acta Mater.* **2013**, *61*, 2163–2178. [CrossRef]
29. Kirchheim, R. Grain coarsening inhibited by solute segregation. *Acta Mater.* **2002**, *50*, 413–419. [CrossRef]
30. Sauvage, X.; Wilde, G.; Divinski, S.V.; Horita, Z.; Valiev, R.Z. Grain boundaries in ultrafine grained materials processed by severe plastic deformation and related phenomena. *Mater. Sci. Eng. A* **2012**, *540*, 1–12. [CrossRef]
31. Löffler, H.; Kovács, I.; Lendvai, J. Decomposition processes in Al-Zn-Mg alloys. *J. Mater. Sci.* **1983**, *18*, 2215–2240. [CrossRef]
32. Liu, J.Z.; Chen, J.H.; Liu, Z.R.; Wu, C.L. Fine precipitation scenarios of AlZnMg(Cu) alloys revealed by advanced atomic-resolution electron microscopy study Part II: Fine precipitation scenarios in AlZnMg(Cu) alloys. *Mater. Charact.* **2015**, *99*, 142–149. [CrossRef]
33. Liu, J.Z.; Chen, J.H.; Yuan, D.W.; Wu, C.L.; Zhu, J.; Cheng, Z.Y. Fine precipitation scenarios of AlZnMg(Cu) alloys revealed by advanced atomic-resolution electron microscopy study Part I: Structure determination of the precipitates in AlZnMg(Cu) alloys. *Mater. Charact.* **2015**, *99*, 277–286. [CrossRef]
34. Komura, Y.; Tokunaga, K. Structural studies of stacking variants in Mg-base Friauf-Laves phases. *Acta Crystallogr. Sect. B* **1980**, *36*, 1548–1554. [CrossRef]
35. Chung, T.-F.; Yang, Y.-L.; Shiojiri, M.; Hsiao, C.-N.; Li, W.-C.; Tsao, C.-S.; Shi, Z.; Lin, J.; Yang, J.-R. An atomic scale structural investigation of nanometre-sized η precipitates in the 7050 aluminium alloy. *Acta Mater.* **2019**, *174*, 351–368. [CrossRef]
36. Li, X.Z.; Hansen, V.; GjØnnes, J.; Wallenberg, L.R. HREM study and structure modeling of the η′ phase, the hardening precipitates in commercial Al–Zn–Mg alloys. *Acta Mater.* **1999**, *47*, 2651–2659. [CrossRef]
37. Ma, Y.; Ahmed, A.; Ji, G.; Zhang, M.X.; Williams, L.; Chen, Z.; Ji, V. Atomic-scale investigation of the interface precipitation in a TiB2 nanoparticles reinforced Al–Zn–Mg–Cu matrix composite. *Acta Mater.* **2020**, *185*, 287–299. [CrossRef]
38. Liu, J.; Hu, R.; Zheng, J.; Zhang, Y.; Ding, Z.; Liu, W.; Zhu, Y.; Sha, G. Formation of solute nanostructures in an Al–Zn–Mg alloy during long-term natural aging. *J. Alloys Compd.* **2020**, *821*, 153572. [CrossRef]
39. Lervik, A.; Thronsen, E.; Friis, J.; Marioara, C.D.; Wenner, S.; Bendo, A.; Matsuda, K.; Holmestad, R.; Andersen, S.J. Atomic structure of solute clusters in Al–Zn–Mg alloys. *Acta Mater.* **2021**, *205*, 116574. [CrossRef]
40. Razazi, H.A.; Paidar, M.; Ojo, O.O. Effect of Mn and Cr on structure and mechanical properties of Al-10%Mg-0.1%Ti alloy. *Vacuum* **2018**, *155*, 619–630. [CrossRef]
41. Wang, Y.; Cao, L.; Wu, X.; Lin, X.; Yao, T.; Peng, L. Multi-alloying effect of Ti, Mn, Cr, Zr, Er on the cast Al-Zn-Mg-Cu alloys. *Mater. Charact.* **2023**, *201*, 112984. [CrossRef]
42. Fattahi, M.; Hsu, C.Y.; Ali, A.O.; Mahmoud, Z.H.; Dang, N.P.; Kianfar, E. Severe plastic deformation: Nanostructured materials; metal-based; polymer-based nanocomposites: A review. *Heliyon* **2023**, *9*, e22559. [CrossRef] [PubMed]
43. Sha, G.; Wang, Y.B.; Liao, X.Z.; Duan, Z.C.; Ringer, S.P.; Langdon, T.G. Influence of equal-channel angular pressing on precipitation in an Al–Zn–Mg–Cu alloy. *Acta Mater.* **2009**, *57*, 3123–3132. [CrossRef]
44. Deschamps, A.; De Geuser, F.; Horita, Z.; Lee, S.; Renou, G. Precipitation kinetics in a severely plastically deformed 7075 aluminium alloy. *Acta Mater.* **2014**, *66*, 105–117. [CrossRef]
45. Jiang, X.J.; Tafto, J.; Noble, B.; Holme, B.; Waterloo, G. Differential scanning calorimetry and electron diffraction investigation on low-temperature aging in Al-Zn-Mg alloys. *Metall. Mater. Trans. A* **2000**, *31*, 339–348. [CrossRef]
46. Richard, D.; Adler, P.N. Calorimetric studies of 7000 series aluminum alloys: I. Matrix precipitate characterization of 7075. *Metall. Trans. A* **1977**, *8*, 1177–1183. [CrossRef]
47. Gubicza, J.; Schiller, I.; Chinh, N.Q.; Illy, J.; Horita, Z.; Langdon, T.G. The effect of severe plastic deformation on precipitation in supersaturated Al–Zn–Mg alloys. *Mater. Sci. Eng. A* **2007**, *460–461*, 77–85. [CrossRef]
48. Legros, M.; Dehm, G.; Arzt, E.; Balk, T.J. Observation of Giant Diffusivity Along Dislocation Cores. *Science* **2008**, *319*, 1646–1649. [CrossRef]

49. Wolverton, C. Crystal structure and stability of complex precipitate phases in Al–Cu–Mg–(Si) and Al–Zn–Mg alloys. *Acta Mater.* **2001**, *49*, 3129–3142. [CrossRef]
50. Berg, L.K.; Gjønnes, J.; Hansen, V.; Li, X.Z.; Knutson-Wedel, M.; Waterloo, G.; Schryvers, D.; Wallenberg, L.R. GP-zones in Al–Zn–Mg alloys and their role in artificial aging. *Acta Mater.* **2001**, *49*, 3443–3451. [CrossRef]
51. Embury, J.D.; Nicholson, R.B. The nucleation of precipitates: The system Al-Zn-Mg. *Acta Metall.* **1965**, *13*, 403–417. [CrossRef]
52. Sha, G.; Cerezo, A. Early-stage precipitation in Al–Zn–Mg–Cu alloy (7050). *Acta Mater.* **2004**, *52*, 4503–4516. [CrossRef]
53. Sha, G.; Cerezo, A. Kinetic Monte Carlo simulation of clustering in an Al–Zn–Mg–Cu alloy (7050). *Acta Mater.* **2005**, *53*, 907–917. [CrossRef]